Research Article | Vol. 25, No. 7 | 3 Apr 2017 | OPTICS EXPRESS 8048

Optics EXPRESS

Separatrix modes in weakly deformed microdisk cavities

CHANG-HWAN YI,[1,2,4] JULIUS KULLIG,[1] JI-WON LEE,[2] JI-HWAN KIM,[2] HYEON-HYE YU,[2] JAN WIERSIG,[1,3] AND CHIL-MIN KIM[2,5]

[1]*Institut für Theoretische Physik, Otto-von-Guericke-Universität Magdeburg, Postfach 4120, D-39016 Magdeburg, Germany*
[2]*Department of Emerging Materials Science, DGIST, Daegu 711-873, South Korea*
[3]*jan.wiersig@ovgu.de*
[4]*changhwan.yi@ovgu.de*
[5]*chmkim@dgist.ac.kr*

Abstract: Optical modes in deformed dielectric microdisk cavities often show an unexpected localization along unstable periodic ray orbits. We reveal a new mechanism for this kind of localization in weakly deformed cavities. In such systems the ray dynamics is nearly integrable and its phase space contains small island chains. When increasing the deformation the enlarging islands incorporate more and more modes. Each time a mode comes close to the border of an island chain (separatrix) the mode exhibits a strong localization near the corresponding unstable periodic orbit. Using an EBK quantization scheme taking into account the Fresnel coefficients we derive a frequency condition for the localization. Observing far field intensity patterns and tunneling distances, reveals small differences in the emission properties.

OCIS codes: (140.3945) Microcavities; (000.1600) Classical and quantum physics.

References and links

1. J. B. Keller, "Corrected Bohr-Sommerfeld quantum conditions for nonseparable systems," Ann. Phys. **4**, 180–188 (1958).
2. H. Waalkens, J. Wiersig, and H. R. Dullin, "The elliptic quantum billiard," Ann. Phys. **260**, 50–90 (1997).
3. M. C. Gutzwiller, "Phase-integral approximation in momentum space and the bound states of an atom," J. Math. Phys. **8**, 1979–2001 (1967).
4. M. C. Gutzwiller, "Energy spectrum according to classical mechanics," J. Math. Phys. **11**, 1791–1806 (1970).
5. M. C. Gutzwiller, "Periodic orbits and classical quantization conditions," J. Math. Phys. **12**, 343–358 (1971).
6. M. Sieber and K. Richter, "Correlations between periodic orbits and their role in spectral statistics," Physica Scripta **T90**, 128–133 (2001).
7. E. J. Heller, "Bound-states eigenfunctions of classically chaotic Hamiltonian systems: Scars of periodic orbits," Phys. Rev. Lett. **53**, 1515–1518 (1984).
8. S. B. Lee, J. H. Lee, J. S. Chang, H. J. Moon, S. W. Kim, and K. An, "Observation of scarred modes in asymmetrically deformed microcylinder lasers," Phys. Rev. Lett. **88**, 033903 (2002).
9. N. B. Rex, H. E. Tureci, H. G. L. Schwefel, R. K. Chang, and A. D. Stone, "Fresnel filtering in lasing emission from scarred modes of wave-chaotic optical resonators," Phys. Rev. Lett. **88**, 094102 (2002).
10. C. Gmachl, E. E. Narimanov, F. Capasso, J. N. Baillargeon, and A. Y. Cho, "Kolmogorov-arnold-moser transition and laser action on scar modes in semiconductor diode lasers with deformed resonators," Opt. Lett. **27**, 824–826 (2002).
11. T. Harayama, T. Fukushima, P. Davis, P. Vaccaro, T. Miyasaka, T. Nishimura, and T. Aida, "Lasing on scar modes in fully chaotic microcavities," Phys. Rev. E **67**, 015207 (2003).
12. W. Fang, A. Yamilov, and H. Cao, "Analysis of high-quality modes in open chaotic microcavities," Phys. Rev. A **72**, 023815 (2005).
13. S.-Y. Lee, J.-W. Ryu, T.-Y. Kwon, S. Rim, and C.-M. Kim, "Scarred resonances and steady probability distribution in a chaotic microcavity," Phys. Rev. A **72**, 061801 (2005).
14. W. Fang, H. Cao, and G. S. Solomon, "Control of lasing in fully chaotic open microcavities by tailoring the shape factor," Appl. Phys. Lett. **90**, 081108 (2007).
15. W. Fang and H. Cao, "Wave interference effect on polymer microstadium laser," Appl. Phys. Lett. **91**, 041108 (2007).
16. S.-B. Lee, J. Yang, S. Moon, J.-H. Lee, K. An, J.-B. Shim, H.-W. Lee, and S. W. Kim, "Universal output directionality of single modes in a deformed microcavity," Phys. Rev. A **75**, 011802 (2007).

#284906 https://doi.org/10.1364/OE.25.008048
Journal © 2017 Received 16 Jan 2017; revised 7 Mar 2017; accepted 7 Mar 2017; published 29 Mar 2017

Optics EXPRESS

17. J. Wiersig and M. Hentschel, "Combining directional light output and ultralow loss in deformed microdisks," Phys. Rev. Lett. **100**, 033901 (2008).
18. J. Wiersig, J. Unterhinninghofen, H. Schomerus, U. Peschel, and M. Hentschel, "Electromagnetic modes in cavities made of negative-index metamaterials," Phys. Rev. A **81**, 023809 (2010).
19. S.-Y. Lee, S. Rim, J.-W. Ryu, T.-Y. Kwon, M. Choi, and C.-M. Kim, "Quasiscarred resonances in a spiral-shaped microcavity," Phys. Rev. Lett. **93**, 164102 (2004).
20. S.-Y. Lee, S. Rim, J.-W. Ryu, T.-Y. Kwon, M. Choi, and C.-M. Kim, "Ray and wave dynamical properties of a spiral-shaped dielectric microcavity," J. Phys. A: Math. Theor. **41**, 275102 (2008).
21. C.-M. Kim, S. H. Lee, K. R. Oh, and J. H. Kim, "Experimental verification of quasiscarred resonance mode," Appl. Phys. Lett. **94**, 231120 (2009).
22. E. G. Altmann, G. Del Magno, and M. Hentschel, "Non-hamiltonian dynamics in optical microcavities resulting from wave-inspired corrections to geometric optics," Euro. Phys. Lett. **84**, 10008 (2008).
23. H. E. Tureci and A. D. Stone, "Deviation from Snell's law for beams transmitted near the critical angle: application to microcavity lasers," Opt. Lett. **27**, 7–9 (2002).
24. J. Wiersig, "Formation of long-lived, scarlike modes near avoided resonance crossings in optical microcavities," Phys. Rev. Lett. **97**, 253901 (2006).
25. J. Unterhinninghofen, J. Wiersig, and M. Hentschel, "Goos-Hänchen shift and localization of optical modes in deformed microcavities," Phys. Rev. E **78**, 016201 (2008).
26. C.-H. Yi, S. H. Lee, M.-W. Kim, J. Cho, J. Lee, S.-Y. Lee, J. Wiersig, and C.-M. Kim, "Light emission of a scarlike mode with assistance of quasiperiodicity," Phys. Rev. A **84**, 041803 (2011).
27. C.-H. Yi, H.-H. Yu, J.-W. Lee, and C.-M. Kim, "Fermi resonance in optical microcavities," Phys. Rev. E **91**, 042903 (2015).
28. C.-H. Yi, J.-H. Kim, H.-H. Yu, and C.-M. Lee, J.-W. Kim, "Fermi resonance in dynamical tunneling in a chaotic billiard," Phys. Rev. E **92**, 022916 (2015).
29. C.-H. Yi, H.-H. Yu, and C.-M. Kim, "Resonant torus-assisted tunneling," Phys. Rev. E **93**, 012201 (2016).
30. E. Ott, *Chaos in Dynamical Systems* (Cambridge U., 1993).
31. A. J. Lichtenberg and M. A. Lieberman, *Regular and Chaotic Dynamics* (Springer, 1992).
32. D. Wisniacki, M. Saraceno, F. J. Arranz, R. M. Benito, and F. Borondo, "Poincaré-birkhoff theorem in quantum mechanics," Phys. Rev. E **84**, 026206 (2011).
33. M. Kalinski and J. H. Eberly, "New states of hydrogen in a circularly polarized electromagnetic field," Phys. Rev. Lett. **77**, 2420 (1996).
34. D. Delande, J. Zakrzewski, and A. Buchleitner, "Comment on new states of hydrogen in a circularly polarized electromagnetic field," Phys. Rev. Lett. **79**, 3541 (1997).
35. D. A. Wisniacki and P. Schlagheck, "Quantum manifestations of classical nonlinear resonances," Phys. Rev. E **92**, 062923 (2015).
36. H. Cao and J. Wiersig, "Dielectric microcavities: Model systems for wave chaos and non-hermitian physics," Rev. Mod. Phys. **87**, 61 (2015).
37. J. Wiersig, "Boundary element method for resonances in dielectric microcavities," J. Opt. A: Pure Appl. Opt. **5**, 53–60 (2003).
38. K. Husimi, "Some formal properties of the density matrix," Proc. Phys. Math. Soc. Jpn. **22**, 264–314 (1940).
39. M. Hentschel, H. Schomerus, and R. Schubert, "Husimi functions at dielectric interfaces: Inside-outside duality for optical systems and beyond," Europhys. Lett. **62**, 636–642 (2003).
40. H. J. Korsch, C. Müller, and H. Wiescher, "On the zeros of the husimi distribution," J. Phys. A **30**, L677 (1997).
41. J. Unterhinninghofen and J. Wiersig, "Interplay of Goos-Hänchen shift and boundary curvature in deformed microdisks," Phys. Rev. E **82**, 026202 (2010).
42. H. E. Tureci, H. G. L. Schwefel, A. D. Stone, and E. E. Narimanov, "Gaussian-optical approach to stable periodic orbit resonances of partially chaotic dielectric micro-cavities," Opt. Express **10**, 752–776 (2002).
43. J. B. Keller and S. Rubinow, "Asymptotic solution of eigenvalue problems," Ann. Phys. **9**, 24–75 (1960).
44. V. I. Arnol′d, *Mathematical Methods of Classical Mechanics*, vol. 60 of *Graduate Texts in Mathematics* (Springer, 1978).
45. L. J. Curtis and D. G. Ellis, "Use of the Einstein-Brillouin-Keller action quantization," Am. J. Phys. **72**, 1521 (2004).
46. M. V. Berry, "Regularity and chaos in classical mechanics, illustrated by three deformations of a circular 'billiard'," Eur. J. Phys. **2**, 91–102 (1981).
47. N. Mertig, J. Kullig, C. Löbner, A. Bäcker, and R. Ketzmerick, "Perturbation-free prediction of resonance-assisted tunneling in mixed regular-chaotic systems," Phys. Rev. E **94**, 062220 (2016).
48. J. Kullig and J. Wiersig, "Q spoiling in deformed optical microdisks due to resonance-assisted tunneling," Phys. Rev. E **94**, 022202 (2016).
49. O. Brodier, P. Schlagheck, and D. Ullmo, "Resonance-assisted tunneling," Ann. Phys. (New York) **300**, 88–136 (2002).
50. J. Wiersig, "Resonance zones in action space," Z. Naturforsch. **57a**, 537–556 (2001).
51. J. Kullig, C. Löbner, N. Mertig, A. Bäcker, and R. Ketzmerick, "Integrable approximation of regular regions with a nonlinear resonance chain," Phys. Rev. E **90**, 052906 (2014).
52. J. Wiersig and M. Hentschel, "Unidirectional light emission from high-Q modes in optical microcavities," Phys.

Optics EXPRESS

Rev. A **73**, 031802(R) (2006).
53. S. C. Creagh and M. M. White, "Differences between emission patterns and internal modes of optical resonators," Phys. Rev. E **85**, 015201 (2012).
54. M. Tomes, K. J. Vahala, and T. Carmon, "Direct imaging of tunneling from a potential well," Opt. Express **17**, 19160–19165 (2009).
55. S.-Y. Lee and K. An, "Directional emission through dynamical tunneling in a deformed microcavity," Phys. Rev. A **83**, 023827 (2011).
56. J.-B. Shim and J. Wiersig, "Semiclassical evaluation of frequency splittings in coupled optical microdisks," Opt. Express **21**, 24240–24253 (2013).
57. J. U. Nöckel and A. D. Stone, "Chaos in optical cavities," Nature (London) **385**, 45–47 (1997).

1. Introduction

The ray-wave (classical-quantum) correspondence has been the objective of extensive research. Semiclassical methods such as the Einstein-Brillouin-Keller (EBK) quantization scheme [1, 2] for integrable systems and trace formulas for the periodic orbits (POs) of classically chaotic systems [3–6] have proven to be remarkably useful. One particular interesting aspect is the phenomenon of "scarring", first observed by Heller in a quantized stadium billiard [7]. It refers to the existence of energy eigenstates with strong concentration along unstable POs of the underlying classical system. In optical microcavities, the localization of optical modes along short unstable POs has been observed experimentally in various kinds of strongly deformed microlasers [8–11]. These observations are of interest because such modes can have relatively high quality factors (long photon lifetimes) even in the presence of chaos since the corresponding PO is located entirely outside the leaky region, which is the region where the condition for total internal reflection is not fulfilled. Numerical simulations indicate that scarring in open systems with chaotic ray dynamics, such as deformed microdisk cavities, is rather the rule than the exception; see, e.g., [12–18].

A related phenomenon observed in deformed microdisk cavities is the appearance of "quasi-scarred modes" showing a strong localization on simple geometric structures with no underlying PO [19, 20]. Lasing on quasiscarred modes has been successfully realized for spiral-shaped InGaAsP microcavity lasers [21]. Quasiscars find a natural explanation in terms of an extended ray dynamics [22] which incorporates Fresnel filtering [23].

Yet another phenomenon is the appearance of "scarlike modes" in systems with marginal stable POs which have been slightly perturbed [24–29]. These states form near avoided resonance crossings as a perturbation parameter is varied. This happens in particular when an integrable system is slightly perturbed [25]. According to the Poincaré-Birkhoff theorem [30,31] the family of marginal stable POs is replaced by pairs of stable and unstable POs. The stable POs are embedded into small islands in phase space. Figure 1 illustrates this situation in the Poincare surface of section (SOS) [31], a section through the full phase space obtained by plotting the intersection points of a set of trajectories with the cavity's boundary. The unstable POs are located on the enclosure of the island which is called separatrix. For very weak deformation the two modes involved in the avoided resonance crossing hybridize such that one mode is located near the stable POs and the other mode near the unstable POs. This scenario can be considered as a quantum version of the Poincaré-Birkhoff theorem [25], see also [32].

In this article, we reveal another type of localization along unstable POs which appears naturally in weakly deformed microdisk cavities. Consider a weakly deformed cavity with a small island chain in phase space, possibly with a scarlike mode localized near the unstable PO. Increasing the deformation further leads to an increasing of the size of the island chain. The phenomenon occurs as a transition process of modes getting into an increasing island chain from the outside. Each time a mode comes close to the separatrix the mode exhibits a strong localization near the corresponding unstable PO. Such a scenario has been predicted already in the context of atomic physics, namely for hydrogen in a circularly polarized electromagnetic

Optics EXPRESS

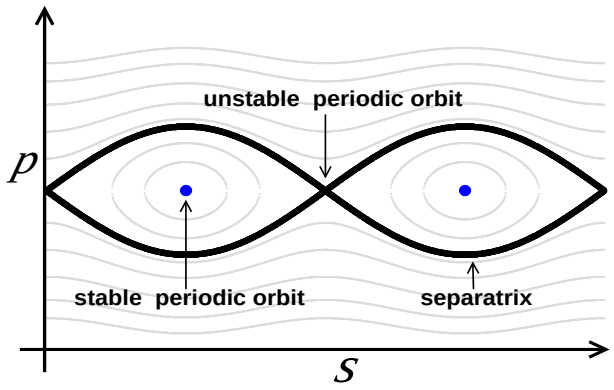

Fig. 1. Sketch of an island chain in the SOS of a near-integrable microcavity. The coordinate s is the arc length along the boundary of the cavity and $p = \sin\chi$ is its canonical conjugate momentum; χ is the angle of incidence. The thin curves are sections through invariant tori. The thick curve marks the separatrix which separates the interior from the exterior of the island chain.

field [33]. Interestingly, the localization at the unstable PO is of classical nature: the classical motion slows down near the unstable point [34]. Similar localization has also been observed in quantum maps [35].

To clarify this localization in our setting, we quantize the POs in terms of a semi-classical approach taking into account the degree of the deformation. Through the analysis, we show that a mode is maximally localized in the vicinity of the unstable PO when its quantized frequency matches the natural frequency of the mode. In addition, by examining intensities outside the cavity, surprising similarity of far field patterns are revealed even though the mode structures, inside the cavity, are completely opposite as in the island and on the separatrix. On the other hand, further studies on the emission properties of these modes near the cavity boundary reveal different tunneling distances of them.

This paper is organized as follows. Section 2 specifies the system that serves as an example. In Sec. 3 we show that this system possesses for very weak deformation the already known scarlike modes. In Sec. 4.1 we semiclassically quantize the unstable PO. Numerical results are presented in Sect. 4.2. A further analysis in terms of a pendulum approximation is given in Sect. 4.3. Section 5 addresses properties of far field intensity patterns. In Sec. 6 tunneling characteristics of emissions are analyzed. The work is summarized in Sect. 7.

2. The system

For our analysis we introduce an oval-shaped cavity

$$x^2 + y^2\,(1 + \varepsilon x) = R^2, \tag{1}$$

where ε is the deformation parameter. For $\varepsilon = 0$ one obtains a circle of radius R. We choose the effective refractive index to be $n_e = 3.3$.

Maxwell's equations are solved in two dimensions within the effective index approximation with Sommerfeld outgoing wave conditions at infinity. The optical modes are defined as the solutions with time dependence $e^{-i\omega t}$. We express the complex-valued frequency ω by the dimensionless frequency $\omega R/c = kR$ where c is the speed of light in vacuum and $k = \omega/c$ is the wave number. The real part of kR is the conventional frequency whereas the imaginary part determines the line width (decay rate) $\gamma = -2\,\mathrm{Im}\,kR$ and the quality factor $Q = -\mathrm{Re}\,kR/[2\,\mathrm{Im}\,kR]$ of the given mode.

Optics EXPRESS

Only in the limiting case $\varepsilon = 0$, the modes can be computed analytically and can be characterized by two mode numbers (l, m), see e.g. [36]. Here, l is the radial mode number and m is the azimuthal mode number. In the general case, the modes are determined numerically. Here, we employ the boundary element method (BEM) [37] and focus on transverse magnetic (TM) polarization, on even modes (positive parity with respect to the symmetry line $y = 0$ of the cavity) and on the regions $95.0 \leq \mathrm{Re}(n_e kR) \leq 96.2$ and $0 \leq \varepsilon \leq 0.05$.

3. Scarlike modes

In this section we demonstrate that for very small ε the oval-shaped cavity (1) possess scarlike modes in the sense of [24]. An example is shown in Figs. 2(a) and 2(b) for $\varepsilon = 0.0025$. Both modes are developed from the $(l, m) = (11, 48)$ and the $(10, 51)$ modes in the circular cavity by continuously increasing ε from 0 to 0.0025.

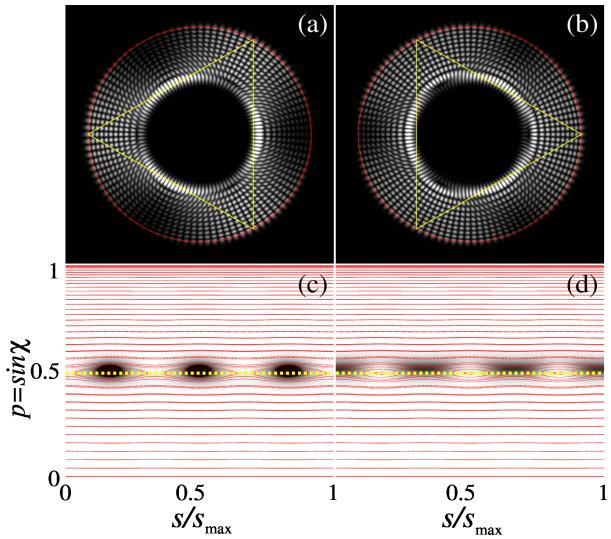

Fig. 2. (a) and (b) Intensity of modes for $\varepsilon = 0.0025$ with dimensionless frequencies $\mathrm{Re}(n_e kR) = 95.726$ and 95.692, respectively. The solid lines mark the stable (a) and the unstable PO (b). (c) and (d) show the corresponding Husimi functions with ray dynamics superimposed. Only the counter-clockwise direction ($p \geq 0$) is shown by virtue of the spatial mirror-symmetry. The localization on a stable and unstable period-3 orbit can be clearly seen. The yellow dashed line at $p = 0.5$ is a guide to the eye.

The connection to the ray dynamics is most conveniently illustrated by the Husimi function [38] of a given mode. It can be considered as quasi-probability distributions of a mode at the boundary of the dielectric cavity [39]. We use here the incidence Husimi function hu(s,p) in the interior region of the cavity [39]. Note that for the Husimi functions we set the squeezing factor ξ of the coherent state as $\sigma' = \xi\sigma = (2\pi/2)(\sqrt{2}/n_e kR)$ [39, 40] in order to reflect our rectangular phase space region $[s_{min}, s_{max}] \times [p_{min}, p_{max}] = [0, 2\pi R] \times [-1, 1]$. Figures 2(c) and 2(d) are Husimi functions of the two modes. By comparing the Husimi functions with the superimposed ray orbits it can be seen that one mode is localized in the island with the period-3 stable PO in its center, whereas the other mode is localized near the period-3 unstable PO. The good agreement between mode and ray calculations may be even improved by incorporating the Goos-Hänchen shift into the ray dynamics [41].

The localization happens when the mode pair satisfies a necessary requirement [25,27] which

Optics EXPRESS

is, essentially, a rational winding number

$$\frac{\omega^l}{\omega^m} = \left|\frac{\Delta n^m}{\Delta n^l}\right| = \frac{r}{t}, \tag{2}$$

where ω^i are classical frequencies of the rays and Δn^i are mode number differences in the i-th degrees of freedom and r and t are integers, respectively. This phenomenon can be understood by the well known Fermi resonance interpretation. In our case, a relation $(\Delta l, \Delta m) = (t, r)$ is used where $\Delta l \equiv \Delta n^l$ and $\Delta m \equiv \Delta n^m$ are the radial and the angular mode number differences. According to this definition, (t, r) represents the classical POs performing r-reflections during t-cyclic motions. In this article, the considered mode pairs have the mode number difference $(\Delta l, \Delta m) = (1, 3)$ and hence the PO should be also $(t, r) = (1, 3)$, which corresponds to the orbits having 3-reflections during 1-rotating motion along the angular direction for a period (i.e., triangular orbit). In fact, we have already observed this relation in the previous example; the $(l, m) = (11, 48)$ mode and the $(10, 51)$ mode at $\varepsilon = 0.0025$ together form the modes that are localized on the period-3 stable and unstable PO, respectively.

4. Separatrix modes

In this section we show that by increasing the deformation further the scarlike mode disappears and that at certain values of the deformation parameter a new type of localized mode appears.

4.1. Periodic orbit quantization

As a first step the period-3 POs are quantized according to an one-dimensional EBK quantization scheme. In analogy to quantum mechanics, we consider the momentum $n_e k$ ($\hbar$ is set to unity) along the entire path of the PO, leading to [42, 43]

$$\oint_l n_e k dl = 2\pi(N + \psi) \tag{3}$$

with the mode number $N = 0, 1, 2, \ldots$ and

$$\psi = \frac{1}{2} + \frac{\mu}{4} + \frac{\phi}{4\pi} + \frac{\alpha}{2\pi}\,. \tag{4}$$

The Maslov index μ counts the number of classical caustics crossed plus twice the number of hard-wall reflections [1, 31, 43–45]. For both period-3 orbits $\mu = 9$ because each orbit crosses the inner caustics three times and gets reflected at the cavity's boundary also three times. The phase ϕ belongs to the monodromy matrix which measures the stability of the PO. In Birkhoff coordinates it is expressed by [46]:

$$\begin{pmatrix}\Delta s_1\\ \Delta p_1\end{pmatrix} = \begin{pmatrix}\frac{\partial s_1}{\partial s_0} & \frac{\partial s_1}{\partial p_0}\\ \frac{\partial p_1}{\partial s_0} & \frac{\partial p_1}{\partial p_0}\end{pmatrix}\begin{pmatrix}\Delta s_0\\ \Delta p_0\end{pmatrix} = M\begin{pmatrix}\Delta s_0\\ \Delta p_0\end{pmatrix}, \tag{5}$$

where $\Delta s_{0(1)}$ and $\Delta p_{0(1)}$ are the initial (final) deviations in s and p axes, respectively. The eigenvalues of the matrix M are $\lambda_\pm = \exp(\pm i\phi)$. For the unstable PO the phase ϕ is zero, because in that case the eigenvalues of the monodromy matrix are purely real. Finally, the Fresnel phase α arises due to the reflection of the ray at the dielectric boundary. From the well-known Fresnel coefficients we get for TM polarization

$$\alpha = \mathrm{Re}\left[-i\sum_{j=1}^{3}\ln\left(\frac{n_e\beta(\chi_j) - 1}{n_e\beta(\chi_j) + 1}\right)\right], \tag{6}$$

Optics EXPRESS

where $\beta(\chi_j) = \cos(\chi_j)/\sqrt{1 - n_e^2 \sin^2(\chi_j)}$. χ_j is the incident angle of the PO at the j-th bouncing point on the cavity's boundary. The quantized frequency is given by

$$n_e kR = \frac{2\pi(N + \frac{1}{2}) + \pi\frac{\mu}{2} + \frac{\phi}{2} + \alpha}{l_{po}/R}, \tag{7}$$

where l_{po} is the length of the given PO. The quantities l_{po}, ϕ, and α are numerically determined depending on the value of the deformation parameter.

4.2. Numerical results

Figure 3(a) shows the quantized frequencies (7) of stable (squares) and unstable (triangles) POs as functions of the deformation parameter ε. Also shown are the modes in the regime $95.0 \leq \mathrm{Re}(n_e kR) \leq 96.2$. The solid line and the dashed one mark the two modes which are developed from the $(11, 48)$ and the $(10, 51)$ mode of the circular cavity. For very small $\varepsilon \approx \varepsilon_1 = 0.002$ their frequencies agree well with the quantized frequencies. Moreover, one of the modes show a strong localization near the unstable PO, (s', p') in phase space, in terms of the averaged Husimi functions $\mathrm{hu}(s', p') = \sum_{n=1}^{3} \mathrm{hu}(s'_n, p'_n)/3$ at that location [see Fig. 3(b)]. This mode is the scarlike mode discussed in Sect. 3.

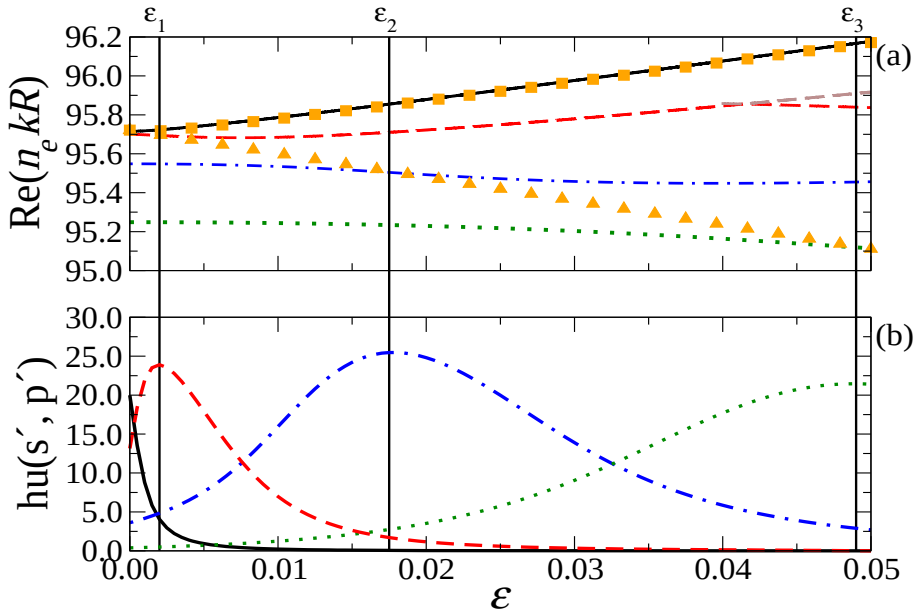

Fig. 3. Dimensionless frequencies (a) and Husimi functions on unstable points (b) related to period-3 POs. The solid, the dashed, the dot-dashed, and the dotted curves originate from the $(l, m) = (11, 48)$, the $(10, 51)$, the $(9, 54)$, and the $(8, 57)$ mode in the circular cavity, respectively. (a) The squares (triangles) are quantized stable (unstable) POs with $N = 76$, see Eq. (7). Vertical lines at $\varepsilon_1 = 0.002$, $\varepsilon_2 = 0.0175$, and $\varepsilon_3 = 0.049$ mark the maximal localization on the unstable PO. There are two kinds of avoided crossings in (a). The first is a broad one along the quantized unstable PO and the second is a sharp one at $\varepsilon \approx 0.0415$. For the sharp one, we focus on the diabatic continuation of the modes by jumping at this point to the other branch.

Upon further increasing the deformation the frequency of the former scarlike modes starts around $\varepsilon = 0.006$ to deviate from that of the quantized unstable PO, Fig. 3(a). This is fully

Optics EXPRESS

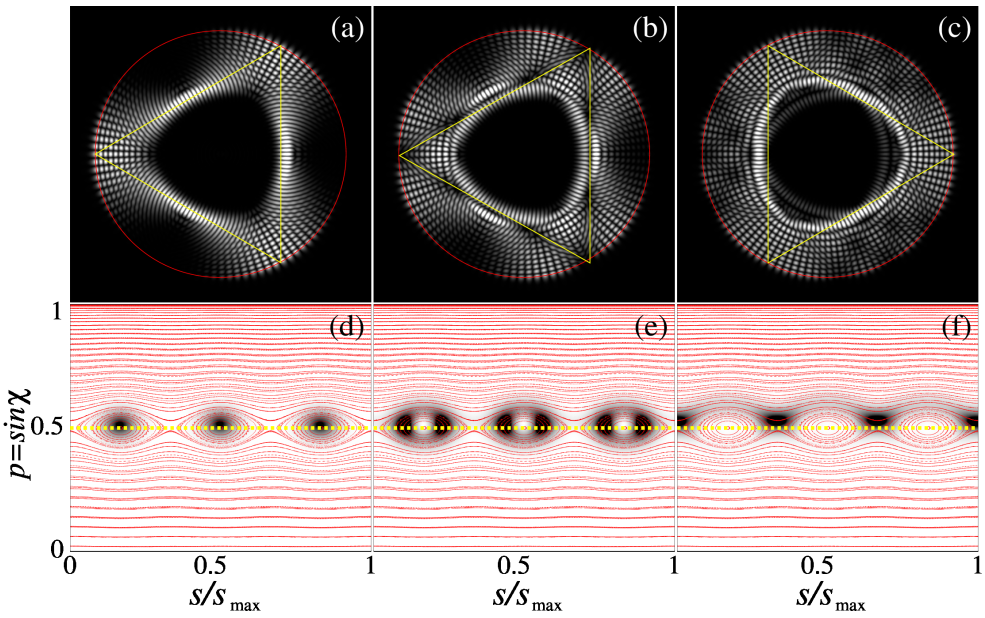

Fig. 4. (a), (b), and (c) Intensity of modes at $\varepsilon = 0.0175$ for the solid, dashed and dot-dashed curves in Fig. 3, respectively. The solid lines mark the stable PO (a)-(b) and the unstable PO (c). (d)-(f) are the Husimi functions of the modes in (a)-(c) superimposed on the SOS (red dots). The yellow dashed line at $p = 0.5$ is a guide to the eye.

consistent with the decrease of localization at the unstable point in Fig. 3(b) at around the same value of ε. The interpretation is that the increasing island swallows up the scarlike mode. It becomes a mode in the island close to the stable PO as it is confirmed in Figs. 4(b) and 4(e). However, in contrast to the mode localized around the stable PO [see Figs. 4(a) and 4(d)], it is localized on a torus surrounding the stable PO. It can be considered as a first excited island mode or as a first transversal excitation of the mode along the stable PO.

As explained, the increasing size of the island chain is responsible for the destruction of the scarlike mode. Interestingly, the very same mechanism gives birth to a new mode being localized around the unstable PO: By increasing the size of the island chain further a new mode comes closer to the separatrix of the island chain until it becomes a "separatrix mode". Since the classical motion becomes very slow near the unstable PO, the separatrix mode mainly has intensity near this unstable PO [see Figs. 4(c) and 4(f)]. This scenario can be observed in Fig. 3. Upon increasing ε the mode originating from the $(9, 54)$ mode of the circular cavity (dot-dashed curve) starts to come closer in frequency to the quantized unstable PO and accumulate intensity at the unstable point. The maximum localization appears at $\varepsilon = 0.0175$.

This mechanism goes now on and on. Upon further increasing the deformation the $(9, 54)$ mode will be incorporated into the island. It is no longer a separatrix mode. On further increasing the deformation the $(8, 57)$ mode (dotted curve in Fig. 3) comes close to the separatrix and shows strong localization near the unstable PO. The maximum localization of this separatrix mode is at $\varepsilon = 0.049$.

The whole progression of creation and annihilation of localization is summarized in Fig. 5. For $\varepsilon \approx 0$ there is no localization along the boundary of the cavity. For $\varepsilon \approx 0.002$ one mode is localized at the stable and one at the unstable PO (scarlike mode). Around $\varepsilon \approx 0.0175$ two modes are located inside the island and one mode is located on the separatrix (separatrix mode) showing large intensity at the unstable PO. For $\varepsilon \approx 0.049$ three modes stay inside the island

Optics EXPRESS

and one on the separatrix.

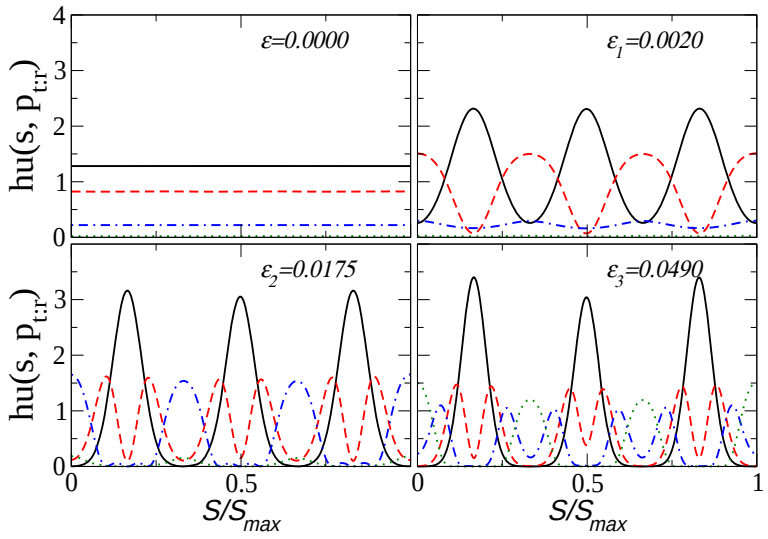

Fig. 5. Husimi functions at $p = p_{t:r}$ for the selected parameters. Solid, dashed, dot-dashed, and dotted curves are for (11,48), (10,51), (9,54), and (8,57) modes of the circular cavity, respectively. Husimi functions are normalized by total intensity in phase space and recorded in an arbitrary unit. The values of ε_1, ε_2, and ε_3 are same as those in Fig. 3.

4.3. *Pendulum approximation*

For a further analysis we consider the pendulum approximation for an isolated island chain in phase space [47–51]

$$H_{t:r}(s,p) = H_0(p) + 2V_{t:r}(\varepsilon)\cos\left(\frac{2\pi r s}{s_{max}}\right) \tag{8}$$

where the unperturbed Hamiltonian H_0 and the strength of potential are

$$H_0(p) = 2\left(p\cos^{-1}(p) - \sqrt{1-p^2} + \sqrt{1-p_{t:r}^2}\right) - \omega(p_{t:r})p \tag{9}$$

$$2V_{t:r}(\varepsilon) = \frac{\sqrt{1-p_{t:r}^2}}{2r^2}\left(\cos^{-1}\left[\frac{Tr\{M_{t:r}(\varepsilon)\}}{2}\right]\right)^2. \tag{10}$$

Here, the frequencies and the momenta of the POs are, respectively, $\omega(p) = 2\cos^{-1}(p)$ and $p_{t:r} = \cos(\pi t/r)$. It should be pointed out that $V_{t:r}(\varepsilon)$ is governed by the trace of the monodromy matrix $M_{t:r}(\varepsilon)$ calculated on the stable (t,r)-PO depending on the deformation parameter ε. From the given Hamiltonian, we estimate a measure of the size of the island chain. In order to figure out this measure we, again, use an approximation in [48, 49, 51] which is optimized to determine the separatrix $p_{sep}(s)$ of the island chain. The size of this separatrix is expressed in terms of momentum distances $\Delta p(s)$ from $p_{t:r}$ as

$$\begin{aligned} p_{sep}(s) &= p_{t:r} \pm \left(2V_{t:r}\sqrt{1-p_{t:r}^2}\left[1-\cos\left(\frac{2\pi r s}{s_{max}}\right)\right]\right)^{\frac{1}{2}} \\ &= p_{t:r} \pm \Delta p(s), \end{aligned} \tag{11}$$

Optics EXPRESS

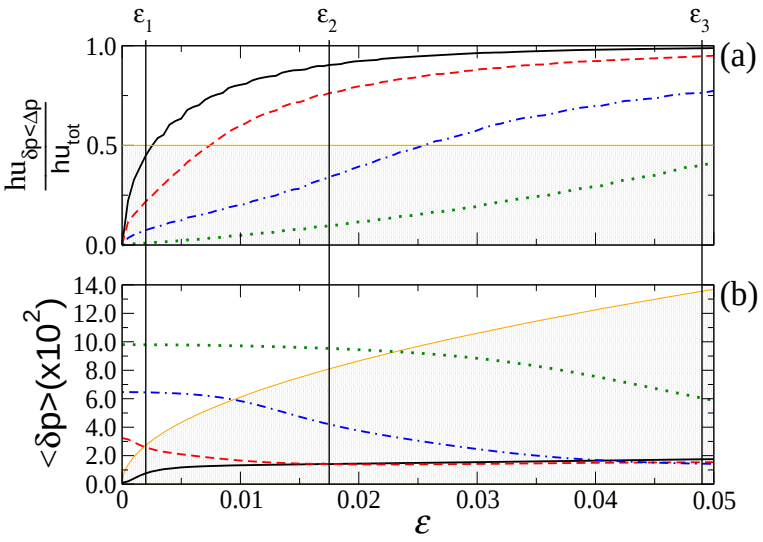

Fig. 6. (a) Ratio of the Husimi functions of the modes from Fig. 3 inside the separatrix normalized by the total Husimi functions on the entire phase space. The shaded region marks values below 1/2. (b) Expectation values of the distances measured from $p_{t:r}$ to p having probabilities hu(s,p). The shaded region indicates values smaller than the width of the island chain from Eq. (11). Vertical lines labeled by ε_1, ε_2, and ε_3 are same as those in Fig. 3.

and the resonance width is given by the maximum value of $\Delta p(s^*)$ which is reached whenever $s^* \equiv s_{max}(2z+1)/2r$ with integer z.

Based on the pendulum approximation, we compute the inside-islands intensities ratio of the Husimi functions as shown in Fig. 6(a). As the deformation parameter increases, the modes are gradually occupying more area in the island chain. The figure confirms the discussed scenario: starting from weak deformation each mode first becomes a separatrix mode with high intensity around the unstable PO [cf. Fig. 3] and low intensity in the island chain [see Fig. 6(a)]. With increasing deformation the localization at the unstable PO reduces and at the same time the intensity in the island chain increases.

Another illustration of the capturing mechanism is shown in Fig. 6(b). The figure shows the expectation value $\langle \delta p \rangle = \int \mathrm{d}s\mathrm{d}p\, \mathrm{hu}(s,p)|p - p_{t:r}| \Big/ \int \mathrm{d}s\mathrm{d}p\, \mathrm{hu}(s,p)$ of the distance from the $p_{t:r}$ using Husimi functions as probability density in phase space and a resonance width using the pendulum approximation. As the deformation parameter increases, the distance of each mode to the island center, $\langle \delta p \rangle$, at some deformation becomes smaller then the size of the island chain, $\Delta p(s^*)$ consistent with Figs. 3 and 6(a).

5. Far fields patterns

Until now, our discussions have been showing no distinct openness feature of the dielectric microcavity. Now, far field emission patterns of the modes are investigated. By these studies, an almost identical directionality is discovered which seemingly not related to the mode localization regions. Figure 7 shows comparisons of far-field intensity patterns between the modes $(l,m) = (11,48)$ localized on the stable points in the islands and successively formed separatrix modes (10,51), (9,54), (8,57) at $\varepsilon = 0.0020, 0.0175, 0.049$, respectively. Hereafter we call the mode $(l,m) = (11,48)$ the island ground mode for convenience.

As we can see in the first row of Fig. 7, emission directions of the island ground and separatrix

Optics EXPRESS

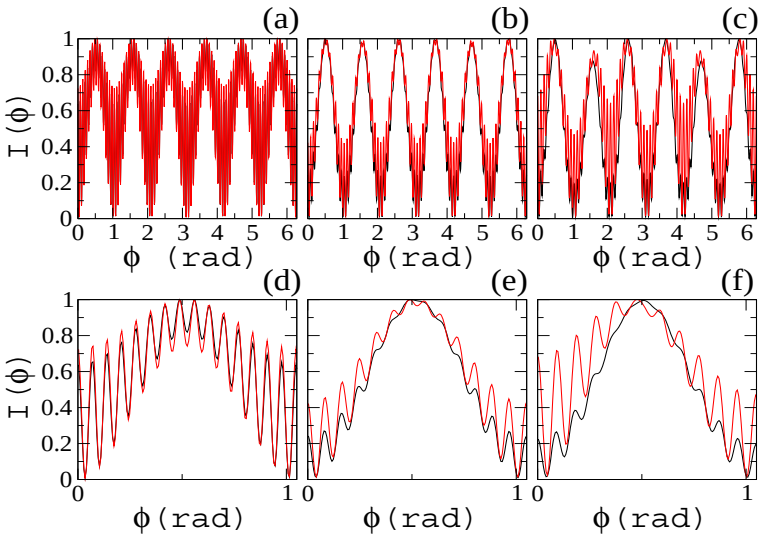

Fig. 7. Angular distributed far-field intensities. (a), (b), and (c) are overlapped far-fields of the island ground and separatrix modes at $\varepsilon_1 = 0.002$, $\varepsilon_2 = 0.0175$, and $\varepsilon_3 = 0.049$. Black curves in all panels are for the island ground modes $(l, m) = (11, 48)$. Red curves in (a), (b), and (c) correspond to the separatrix modes $(10, 51)$, $(9, 54)$, and $(8, 57)$. (d), (e), and (f) are expanded plots of the first prominent lobes of (a), (b), and (c), respectively.

modes are difficult to discern. This surprising similarity of the far fields can be conceived via the phase space distributions of the modes. It is instructive to point out that there are some achievements to hybridize a directional low-Q mode with a high-Q weak directional mode [52]. The back bone of this idea is based on the superposition property of the modes at the avoided resonance crossing point and in that sense the avoided resonance crossing may serve the similar far field patterns of the interacting modes. However, the modes we are discussing in the present paper do not belong to that case since the similarity of the far field patterns is not restricted to the avoided resonance crossing point at all. It is more clear when we see, e.g., Figs. 7(c) and 7(f) which are the far fields of the modes having a large frequency difference at ε_3 in Fig. 3.

It is obvious that a tunneling path from the localization points to the emission regions would take the shortest distance to the critical line of the leaky region. Thus, an emission tail takes the straight extension toward the critical line for the island ground mode while the tail of the separatrix mode occurs at the lowest point of the separatrix in phase space, which are at the same phase space coordinate s as the island mode.

Figure 8 shows Husimi functions of the island ground (above row) and separatrix (below row) modes. In the above row, the three straight stretched Husimi functions from the main localization regions to the critical line are evident while the below row exhibits emission tongues at the same s to the above row which are different from the main localization of the separatrix mode. Note that this mismatch between localization inside the cavity and the emission characteristics outside has already been treated in a different system exhibiting a similar phase space structure [53]. However we emphasize that their works are based on the perturbative treatment of complex ray orbits to describe the emission process while the main focus of the present paper is on the properties of the separatrix mode formation process depending on the deformation parameter.

Optics EXPRESS

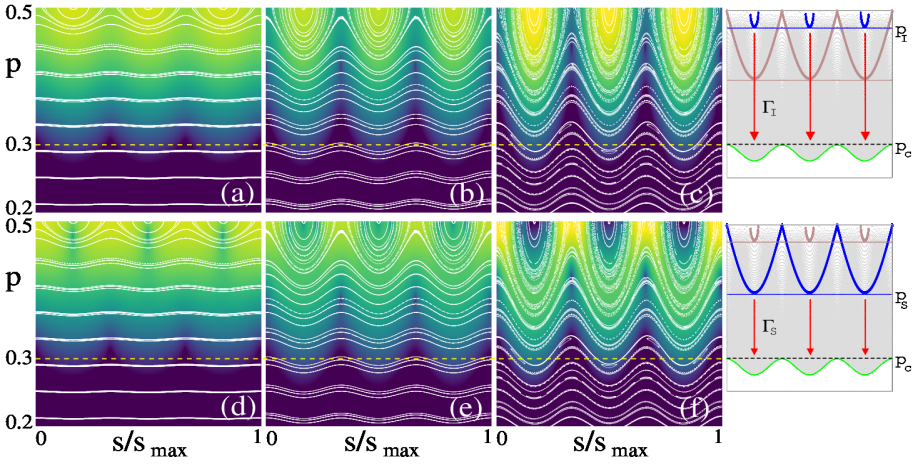

Fig. 8. Logarithmic plot of Husimi functions of the island ground and separatrix modes. (a), (b), and (c) are for the island modes $(l, m) = (11, 48)$ at $\varepsilon_1 = 0.002$, $\varepsilon_2 = 0.0175$, and $\varepsilon_3 = 0.049$, respectively. (c), (d), and (e) are, respectively, for the separatrix modes $(10, 51)$, $(9, 54)$, and $(8, 57)$ at the same deformation in the same column. Dashed lines correspond to the critical line $p_c = 1/n_e \approx 0.303$. Rightmost panels illustrate the tunneling paths of the modes in the same rows. $p_{I(S)}$ and $\Gamma_{I(S)}$ correspond to the tunneling starting point and distance of the island ground (separatrix) mode. The maximum and minimum values of the Husimi functions are shown in yellow and black.

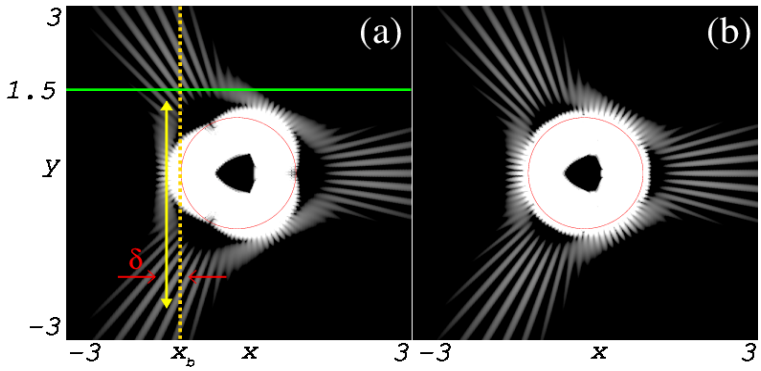

Fig. 9. Logarithmic plot of the intensity. (a) and (b) are the island ground mode (l, m)=(11,48) and the separatrix mode (8,57) at ε_3, respectively. In (a), a horizontal solid line at y=1.5 is a plane for the emission Husimi function. The vertical line at $x = x_b$ is a guide for the left end of the cavity boundary. A line with arrow heads at both ends in (a) visualizes the departure point, remote from x_b, and the radiation directions. All quantities are in units of R.

6. Tunneling distances

In this section, we will address differences of tunneling emission distances of the modes which are measured from the cavity boundary. The distant emission from the cavity boundary is caused by the evanescent leakage fulfilling an angular momentum continuation across the cavity boundary [54–56]. The tunneling distance is given as

$$\begin{aligned} \delta &= R(n_e \sin\chi - 1) \\ &= n_e R(p - p_c) = n_e R\Gamma_p, \end{aligned} \tag{12}$$

Optics EXPRESS

where $p_c = 1/n_e$ is the critical line of the leaky region in phase space. The quantity $\Gamma_p = p - p_c$ is a tunneling distance from p to p_c in phase space (cf. Fig. 8) while δ is a real space distance of the emission point measured from the cavity boundary.

Now, we recall the previous discussions that the emissions of the island ground mode and the separatrix mode share the same emission regions because the separatrix modes tunnel from the lowest points of the separatrix contours in phase space. Consequently, Γ_S of the separatrix mode is smaller than Γ_I of the island ground mode (see rightmost panels in Fig. 8) so that, from Eq. (12), we can expect the smaller δ for the separatrix mode than that of the island ground mode. In order to verify this claim we use, first, Lee's "emission Husimi function" [55] which manipulates a sum of Gaussian overlap of the wave function and its derivative with respect to a certain virtual plane in the exterior region of the cavity. For the emission Husimi function we set the plane at $y_0 = 1.5R$ to detect the field emitting vertically from the left end of the cavity boundary x_b. In Fig. 9(a), this emission direction is guided by a vertical line with arrows and we can see the emission is parallel to the cavity boundary. By comparing all the emissions in Figs. 9(a) and 9(b) we can confirm the very similar emission behaviors of the island ground and separatrix modes again. In the followings we concentrate on the tunneling distances of the vertical emissions radiating from the left end of the cavity boundary.

The emission Husimi function $\tau(x)$ for our setup is :

$$\tau(x) = \left| \int dx' \Phi(x') G(x, x') \right|^2, \tag{13}$$

where $\Phi(x) = 0.5 \left[\psi(x, y_0) - i \partial_y \psi(x, y_0)/k \right]$ and $G(x, x') = 1/(\sigma\pi)^{1/4} \exp\left[-(x - x')^2/2\sigma \right]$. Here $\psi(x, y_0)$, ∂_y, and σ are the wave function along x-axis at fixed $y = y_0$, partial derivative with respect to y and width factor of the Gaussian set to $\sigma = \sqrt{2}/k$ for the wave number k.

Figure 10 exhibits the comparisons of $\tau(x)$ between the island ground and separatrix modes in Fig. 7. From the behavior of the peak position of $\tau(x)$, we can observe two kinds of characteristics of the tunneling distances. The first one is a decreasing tendency of the tunneling distances in both modes as the deformation increases and the other one is an increasing difference of the tunneling distances between the modes depending on the increasing deformations. These are organized in Table 1 and explained below.

Table 1. Tunneling distance (measured in units of R) depending on deformation ε. δ_I, δ_S, and $\Delta\delta$ are the tunneling distance of the island ground mode, of the separatrix modes and the difference of them, respectively. The second and third columns are obtained from the peak positions of Fig. 10 and Eq. (15).

ε	δ_I - δ_S = $\Delta\delta$	δ_I^f - δ_S^f = $\Delta\delta^f$
0.0020	0.538 - 0.522 = 0.016	0.560 - 0.555 = 0.005
0.0175	0.358 - 0.310 = 0.048	0.356 - 0.326 = 0.030
0.0490	0.270 - 0.194 = 0.076	0.228 - 0.178 = 0.050

When the deformation is very weak Γ_I and Γ_S are either close to the resonant torus $\sin\chi = 0.5$ corresponding to $\delta = 0.65R$ when certain modes are on the torus. For strong deformation, the more curved KAM tori [57] result in smaller Γ_I and Γ_S. Consequently, tunneling distances, in real space, have relatively closer values to $0.65R$ for small deformation and decrease toward zero following the increasing deformation as we can perceive in Table 1.

As a final remark we relate the far field intensities of Fig. 7 and the near field tunneling distances. By taking a Fourier transform of the far field intensity pattern, we can obtain an

Optics EXPRESS

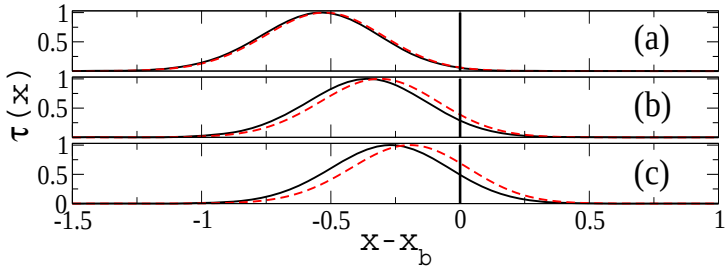

Fig. 10. Emission Husimi function $\tau(x)$ with the setup described in Fig. 9(a). Solid and dashed curves in (a), (b), and (c) correspond to the island ground mode (l, m) =(11,48) and the separatrix mode (8,57) at $\varepsilon = \varepsilon_1 = 0.002$, $\varepsilon_2 = 0.0175$, and $\varepsilon_3 = 0.049$, respectively. Horizontal and vertical axes are scaled in R and arbitrary unit, respectively.

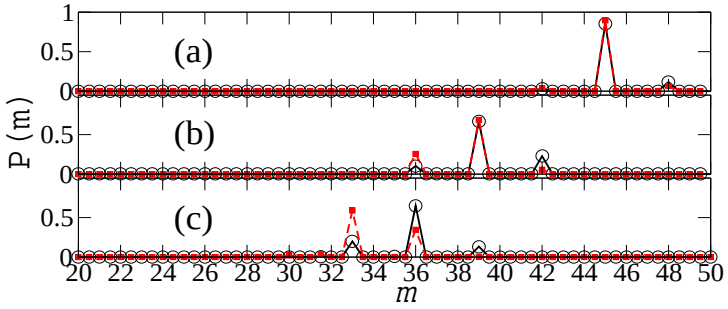

Fig. 11. Weight function $P(m) = |\mathcal{F}(m)|^2$ versus angular momentum number m of the far field intensity. Open circle with solid lines and filled square with dashed lines are for the island ground and separatrix modes. (a), (b), and (c) are at $\varepsilon_1 = 0.002$ $\varepsilon_2 = 0.0175$, and $\varepsilon_3 = 0.049$, respectively.

amplitude of an angular momentum number m as

$$\mathcal{F}(2m) = \frac{1}{\mathcal{Z}} \int \mathrm{d}\phi \, I(\phi) e^{im\phi} \tag{14}$$

$$\mathcal{Z} = \sum_{m_i}^{m_f} |\mathcal{F}(2m)|^2.$$

A factor 2 of the argument at the left hand side in Eq. (14) reflects the fact the Fourier transform is applied to the field intensity $I = |\psi|^2$ not amplitude ψ for the purpose of mimicking the practical measurement. A normalizing factor $\mathcal{Z}$ is introduced in order to manipulate a square absolute value of $\mathcal{F}(m)$ as a weight function of m, i.e., $P(m) = |\mathcal{F}(m)|^2$. Note that by comparing the Fourier transform of the wave amplitudes and of the wave intensities, we have observed significant additional side peaks in the intensity case (not shown), in particular, around $m = 3$ corresponding to the 6 maxima in the far field intensity pattern. Thus, in order to abandon the effects from these contributions we consider only the range from $m_i = 20$ to $m_f = 50$.

Figure 11 shows weight functions of the far field intensities in Fig. 7 with respect to the angular momentum number m. According to the increasing deformation, from Figs. 11(a) to (c), a clustered distribution of m moves from high to low values for both modes while the distributions in the clusters are individually changing. Using this weight function, we can obtain

Optics EXPRESS

the tunneling distances in Eq. (12) with averaged values of $\sin\chi = m/n_e kR$ as below

$$\delta^f = \frac{1}{k}\left[\sum_{m_i}^{m_f} mP(m) - kR\right]. \tag{15}$$

The results in the third column of Table 1 are nicely but not perfectly matching with the estimations of the emission Husimi functions. On this stage it is unclear how much and what kind of errors are there in both approaches since we did not carry out the intensive error analysis . However, it looks that significant information of tunneling process is embedded in the far field intensity patterns.

7. Summary

We presented a new type of mode localization along unstable periodic orbits in deformed microdisk cavities. In the regime of weak deformation the near-integrable ray dynamics exhibits small island chains in phase space. When increasing the deformation the enlarging islands incorporate more and more modes. Each time a mode comes close to the separatrix of the island chain the mode exhibits a strong localization near the associated unstable periodic orbit.

We demonstrated this interesting effect by studying an oval-shaped cavity. For very weak deformation this cavity exhibits the conventional scarlike modes. We showed that by increasing further the deformation the revealed mechanism first destroys the scarlike mode and then subsequently creates and destroys the new type of localized separatrix modes. Using an EBK quantization scheme for the periodic orbits we derive a frequency condition for the localization. The mode shows the localization whenever its frequency is comparable to that of the quantized frequency of the unstable periodic orbit.

Through the investigations of the mode emission properties, very similar far field intensities and different tunneling distances are revealed.

Funding

This research was supported by High-Tech Convergence Technology Development Program (NRF-2014M3C1A3051331) through the National Research Foundation of Korea (NRF) funded by the Ministry of Science, ICT & Future Planning and the DFG (project WI1986/7-1).